CHAPTER 7

STRUCTURAL, DIELECTRIC, FERROELECTRIC AND IMPEDANCE SPECTROSCOPIC STUDIES ON $BaTi_{1-x}Sn_xO_3$ (x=0.05, 0.10, 0.15)

7.1 Introduction

$BaTi_{1-x}Sn_xO_3$ (BTS) is a solid solution of ferroelectric barium titanate and non ferroelectric barium stannate. $BaTi_{1-x}Sn_xO_3$ has promising properties that can be used for various applications such as sensors, piezoelectric actuators or high permittivity dielectric devices, multilayer capacitors, photoluminescence, non-volatile memories and pyroelectric detectors, tuneable microwave devices etc. This material has attracted considerable interest recently due to its promising electrocaloric properties that can be used for development of eco-friendly room–temperature refrigeration systems and cooling devices [Upadhyay et al. (2014)]. Strong electrocaloric effect was observed by Luo et al. (2014) near the composition x = 0.105 (called x_c) which corresponds to the quasi-quadruple critical point of the cubic–tetragonal– orthorhombic–rhobohedral phase transition sequence in the phase diagram. At this composition they have observed greatly enhanced electrocaloric effect near room temperature (~28 ^{0}C) which is very promising for developing cooling devices. However there are varying reports about the composition where permittivity is maximum.

BTS has stable ferroelectric properties in the vicinity of Curie point and the behaviour becomes more relaxor like as Sn content increases. Zhang et al. (2015) have studied this material for 0.1 < x < 0.18 (x = 0.1, 0.12, 0.15, 0.18) and reported DPT

behaviour. They observed fairly wide electrocaloric operating temperature range near room temperature for x = 0.18. Markovic et al. (2010) have prepared samples using x = 0.025, 0.05, 0.07, 0.10 and 0.15 and found that structure remains tetragonal upto x = 0.10 and becomes cubic for x = 0.15. In yet another report they had observed phase becoming cubic at x=0.12 [Markovic et al. (2007)]. Study of dielectric behaviour has been carried out by Shvartsman et al. (2006) using samples with x= 0.10, 0.15 and 0.20. They find that the system remains ferroelectric with $x \leq 0.15$ and dielectric permittivity attains maximum value when x = 0.15 and relaxor behaviour is observed for x=0.20. Lei et al. (2007) studied temperature dependence of permittivity for x = 0.06, 0.12, 0.18, 0.20, 0.30 and found that relaxor behaviour appears for $x > 0.19$. Zhang et al. (2014) studied samples with x = 0.01, 0.03, 0.05 and found that permittivity was maximum for x =0.03. Mueller et al. (2004) observed deviation from Curie-Weiss law (that is specific for relaxor ferroelectrics) in a narrow temperature region above Curie point even when $BaSnO_3$ content (x) is between 0.10 and 0.20. It has been reported that dielectric constant attains a maximum value for x = 0.15 [Shvartsman et al.(2006)].

Upadhyay et al.(2014) reported P-E measurements for x= 0.02, 0.05 and 0.10 and found high electrocaloric effect at low field for x = 0.05. $BaTi_{1-x}Sn_xO_3$ ceramic has shown high value of tuneability and has been projected as material having a potential to replace the so popular $(Ba,Sr)TiO_3$ in microwave applications [Lu et al.(2004)]. They studied the system for x = 0.1, 0.2, 0.3, 0.4 and observed that 54% tuneability can be achieved which decreases as x is increased.

As the useful properties of this system has been attributed to arise for compositions close to the four-phase quadruple point x_c (~ 0.11), it was considered worthwhile to prepare this material with values x = 0.05 (ie < x_c), x = 0.10 (ie ~ x_c) and x=0.15 (ie > x_c) and characterize by XRD, SEM, EDS, impedance spectroscopy, P-E measurement and dielectric measurements at RF and microwave frequencies. This would be useful in developing an overall understanding of various processes present in the system.

7.2 Experimental

The system $BaTi_{1-x}Sn_xO_3$ (denoted as BTS5 (x = 0.05), BTS10 (x = 0.10) and BT15 (x = 0.15) prepared by conventional solid state route. High purity powders of $BaCO_3$, SnO_2 and TiO_2 (Merck 99.5%) were mixed thoroughly by ball milling in zirconia media for 6 hours. They were calcined at 1150 ^{0}C for 6 hours. The calcined powders were mixed with small amount of Polyvinyl alcohol (PVA) binder and pressed into disc-like (dia 12 mm, thickness 1.5 mm) and rectangular (23 mm x 10 mm x 4 mm) pellets using uniaxial hydraulic press under 60 kN load. The pellets were heated slowly (@ 2 ^{0}C/min) to 500 ^{0}C and kept for an hour to burn off the binder. Then the temperature was raised to 1300 ^{0}C by heating at the rate of 5 ^{0}C/min in an electrically heated furnace (Lenton, Germany) and maintained at this temperature for 6 hrs. There after the samples were cooled at the rate of 5^{0}C/min to room temperature.

X-ray diffraction (XRD) patterns were recorded at room temperature to confirm phase formatiom of the calcined and sintered powders using a Rigaku high resolution X-ray diffractometer employing Cu K_α radiation with Ni-filter in the diffraction angle (2θ) range 20º- 90º using a slow scan rate. Rietveld refinement was carried out using Fullprof software. Experimental (bulk) density of the samples was determined by

Archimedes principle and percentage porosity was calculated using the formula:

$$\% \text{ porosity} = \frac{\text{theoretical density} - \text{experimental density}}{\text{theoretical density}} \text{ x } 100$$

Scanning Electron Microscope (ZIESS) was used to study the surface morphology. For this, the sintered pellets were thoroughly polished using emery papers of grade 1/0 (40 μm), 2/0 (30 μm), 3/0 (20 μm) and 4/0 (10 μm) (Sia, Switzerland). The fine polishing was done on blazer cloth using 0.25 μm diamond paste of grade 1/4-OS-475 (HIFIN). The pellets were then thermally etched at a temperature 100 ^{0}C lower than the sintering temperature for about 15 minutes to delineate the morphology. The etched pellets were then gold coated.

Dielectric and impedance measurements were carried out in the frequency range 1 Hz – 1 MHz from 300 - 723 K by using Novocontrol Alpha-A Analyzer. For this the disc like cylindrical pellets were polished using emery papers of grade 1/0 and 2/0 and electroded on both sides using silver paste which was cured at 600 ^{0}C for 15 minutes. Similar electroded pellets were used to measure the P-E hysteresis loops using the instrument AixACCT systems TF Analyzer 2000E, Germany. The high frequency dielectric measurements were carried out at room temperature in X-Band (8.2 GHz – 12.4 GHz) using the Keysight E5071C Network Analyzer. The rectangular pellets were placed in the X-Band rectangular waveguide which was connected to the Network Analyzer through a coaxial cable using a coaxial to waveguide adapter. The measurement technique is based on the so-called transmission line method (Nicolson-Ross-Weir method) which involves placing the sample inside a portion of an enclosed transmission line (in the present system, metallic rectangular waveguide) and measuring scattering parameters S_{11} and S_{21} which are used to obtain the dielectric properties of the material [Nicolson et al 1970, Weir 1974]. The details have been mentioned in section 3.2.5 of chapter 3 and Appendix A.

7.3 Results and Discussion

7.3.1 Phase analysis

Figure 7.1 (a) shows the X-Ray diffraction (XRD) patterns for all the samples. The patterns for x=0.05 and 0.10 match well with the JCPDS 79-2264 (space group P4mm) while for x=0.15, with JCPDS 75-0212 (space group Pm3m) without any impurity phase peaks. Fig. 1(b) shows the 211 peak around $2\theta = 56^0$ for all the samples. There is a slight shoulder on the right side of the 211 peaks which is nothing but $K\alpha_2$ component of X-rays. The peak positions shift towards lower 2θ as the Sn content increases. This is due to increase in the lattice parameters by substitution of the bigger Sn^{4+} (ionic radius r_i=0.83 Å) [Shannon 1969] on Ti^{4+} (ionic radius r_i=0.74 Å) [Lijuan et al. (2013); Markovic et al. (2007)].

Rietveld refinement (shown in Figs. 1(c-e)) confirms these observations as the lattice parameters along with the unit cell volume $V(Å)^3$ increase with increase in Sn content while the c/a ratio decreases and reaches 1 for x=0.15, as given in Table 7.1. This shows decrease in tetragonality as Sn content increases which is in agreement with the results of markovic et al. (2007) and chang et al. (1998).

Table 7.1: Rietveld refinement parameters

x	a(Å)	c(Å)	c/a	$V(Å)^3$	Bragg R-factor	χ^2	Experimental Density (gm/cc)	% Porosity
0.05	4.009	4.018	1.002	64.58	1.75	2.49	5.15	5.21
0.10	4.015	4.022	1.001	64.84	2.01	1.62	5.47	5.56
0.15	4.024	4.024	1.000	65.15	1.51	2.61	5.29	7.47

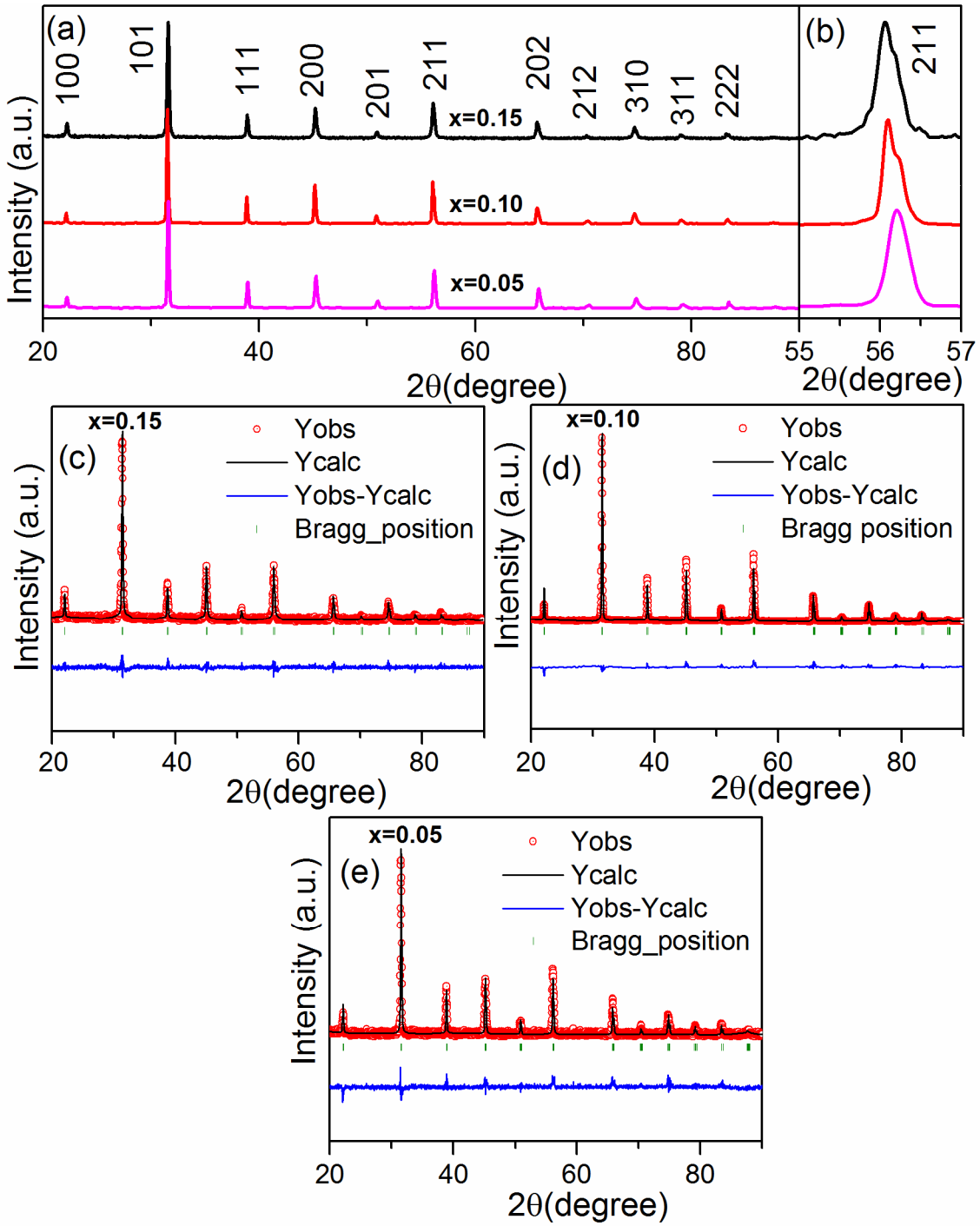

Figure 7.1: (a) XRD patterns for $BaTi_{1-x}Sn_xO_3$ (x = 0.05, 0.10 and 0.15), (b) Magnified peaks around 56 degree, Rietveld refinement for (c) x=0.05, (d) x=0.10 and (e) x=0.15

7.3.2 Microstructure and Energy Dispersive Spectroscopy

The Scanning Electron Micrographs taken at 20,000 X magnification are presented for the samples in Figures 7.2(a-c). The SEM micrographs show the presence of well faceted and uniform polyhedral grains with minimal voids. Aggregation of fine particles have led to grains formation of regular shape morphology throughout all the compositions. The average grain size for BTS5, BTS10 and BTS15 are 4 μm, 2.5 μm and 1.5 μm respectively. There is a clear trend of reduction of grain size with increase in tin content.

The EDS plots for all the compositions are shown in figures 7.3-7.5. The EDS was taken at the grain, grain boundary and overall area. It is seen that more of Sn gets segregated in the grain boundaries as compared to grains. Table 7.2 presents the weight and atomic fractions of the above elements obtained from EDS. They match closely with the expected values from the initial composition.

Table 7.2: EDS results for $BaTi_{1-x}Sn_xO_3$ (x = 0.0, 0.10 and 0.15)

Composition	Ba		Ti		Sn		O	
	Wt %	**At%**	**Wt %**	**At%**	**Wt %**	**At%**	**Wt %**	**At%**
x=0.05	58.30	20.10	19.18	18.97	2.59	1.03	20.24	59.90
x=0.10	58.21	20.07	17.89	17.96	5.04	2.04	19.96	59.93
x=0.15	56.21	19.96	16.67	16.98	7.35	3.02	19.70	60.04

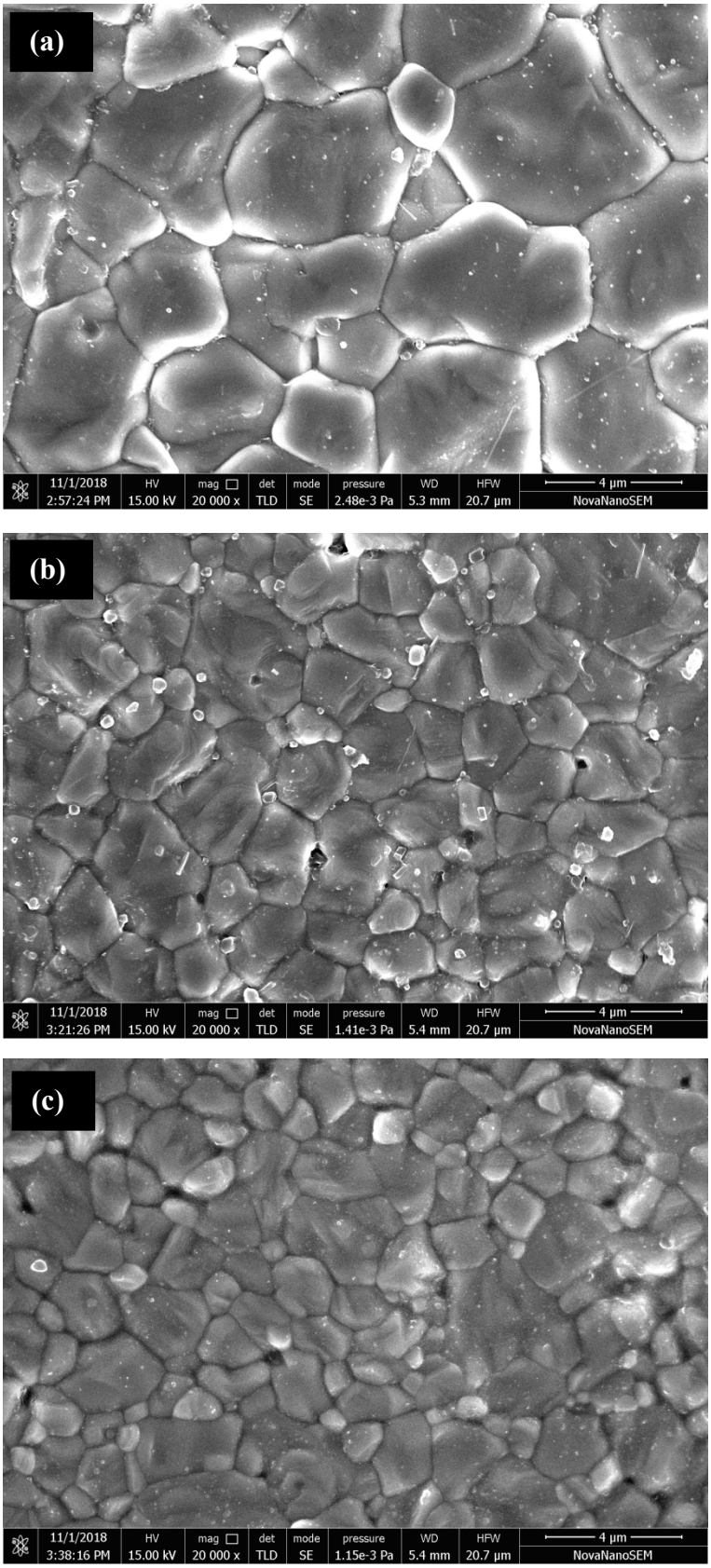

Figure 7.2: SEM micrographs for $BaTi_{1-x}Sn_xO_3$ (a) x = 0.05, (b) x = 0.10, (c) x = 0.15

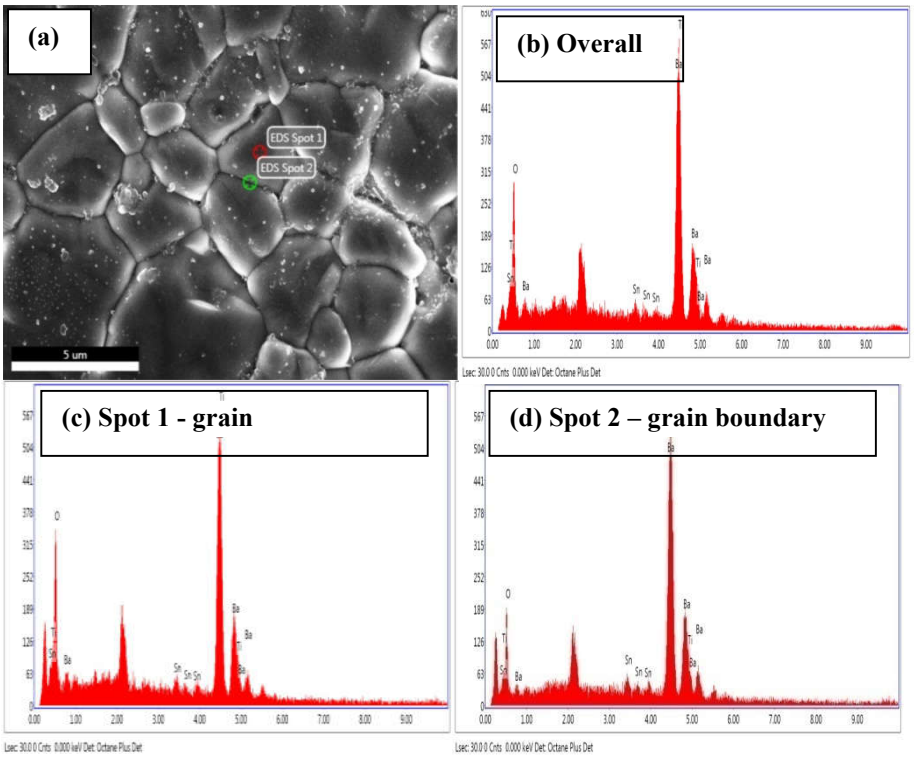

Figure 7.3: (a) SEM micrographs, EDS spectra at (b) Overall area, (c) grain and (d) grain boundary for $BaTi_{1-x}Sn_xO_3$ (x = 0.05)

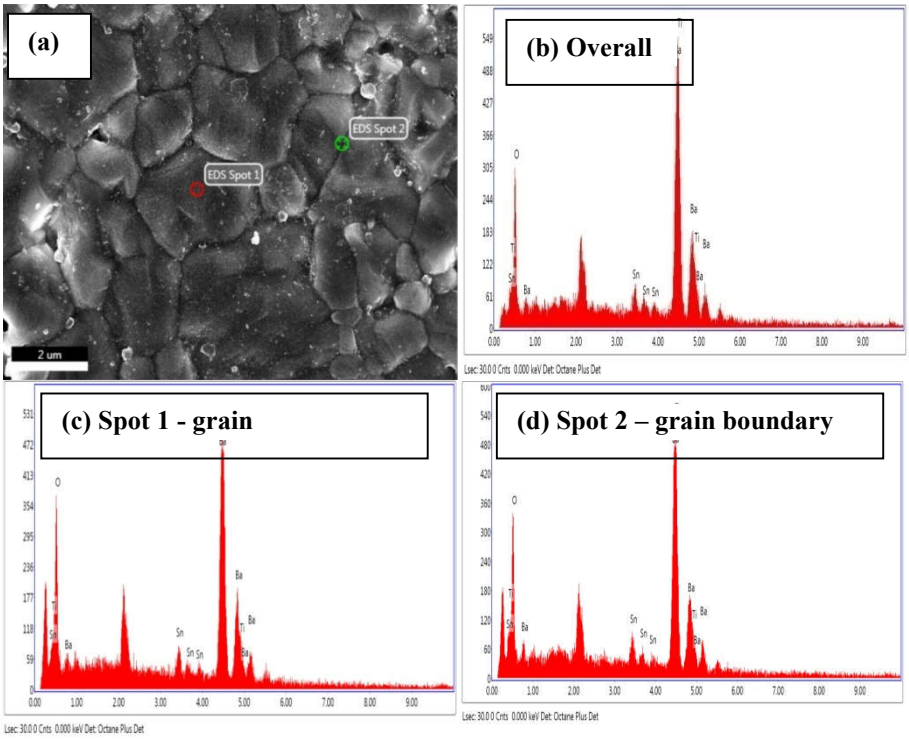

Figure 7.4: (a) SEM micrographs, EDS spectra at (b) Overall area, (c) grain and (d) grain boundary for $BaTi_{1-x}Sn_xO_3$ (x = 0.10)

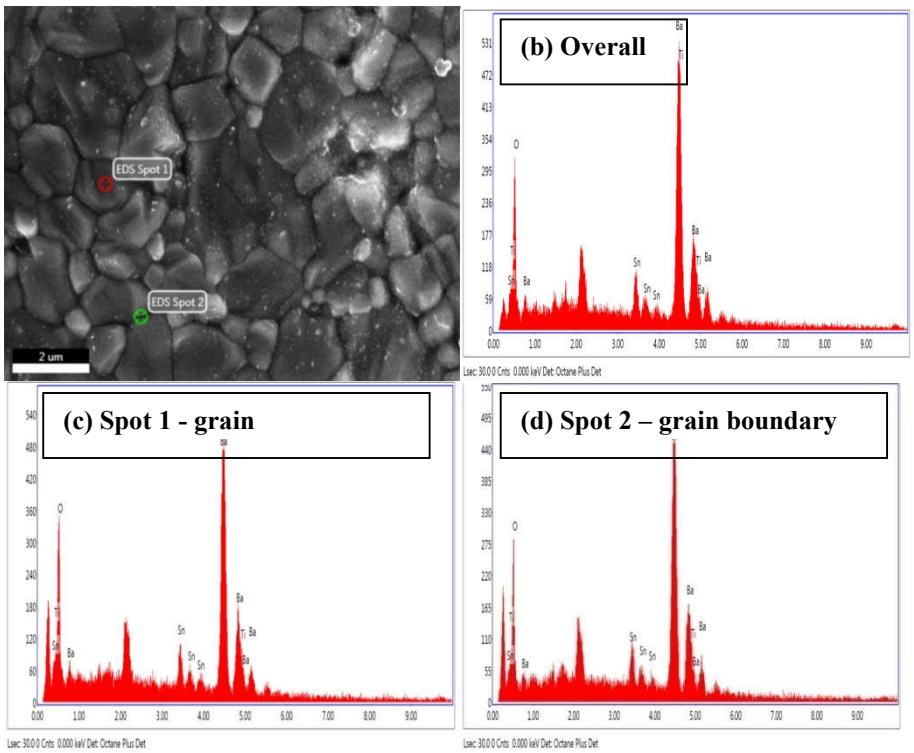

Figure 7.5: (a) SEM micrographs, EDS spectra of (b) Overall area, (c) grain and (d) grain boundary for $BaTi_{1-x}Sn_xO_3$ (x = 0.15)

7.3.3 Dielectric characterization (RF Range)

Typical plots for permittivity (ε′) vs. temperature, permittivity(ε′) vs. frequency, loss tangent vs. temperature and loss tangent vs. frequency for all the samples are shown in Figures 7.6, 7.7 and 7.8. Values of maximum permittivity (ε'_m), the corresponding temperature T_m, room temperature values of permittivity (ε'_{RT}) and loss tangent at 1 MHz for all the samples are given in Table 7.3. It is evident from Table 7.3 that addition of Sn doping leads to increase in permittivity (ε′) [markovic et al. 2007]. BTS15 however has lower value for the same as its phase transition temperature. The peak temperature T_m is seen to decrease with increase in Sn content. This can be attributed to formation of non-ferroelectric SnO6 octahedra which disrupt the cooperative linking between the ferroelectric TiO6 octahedra [Baskaran et al. (2001)].

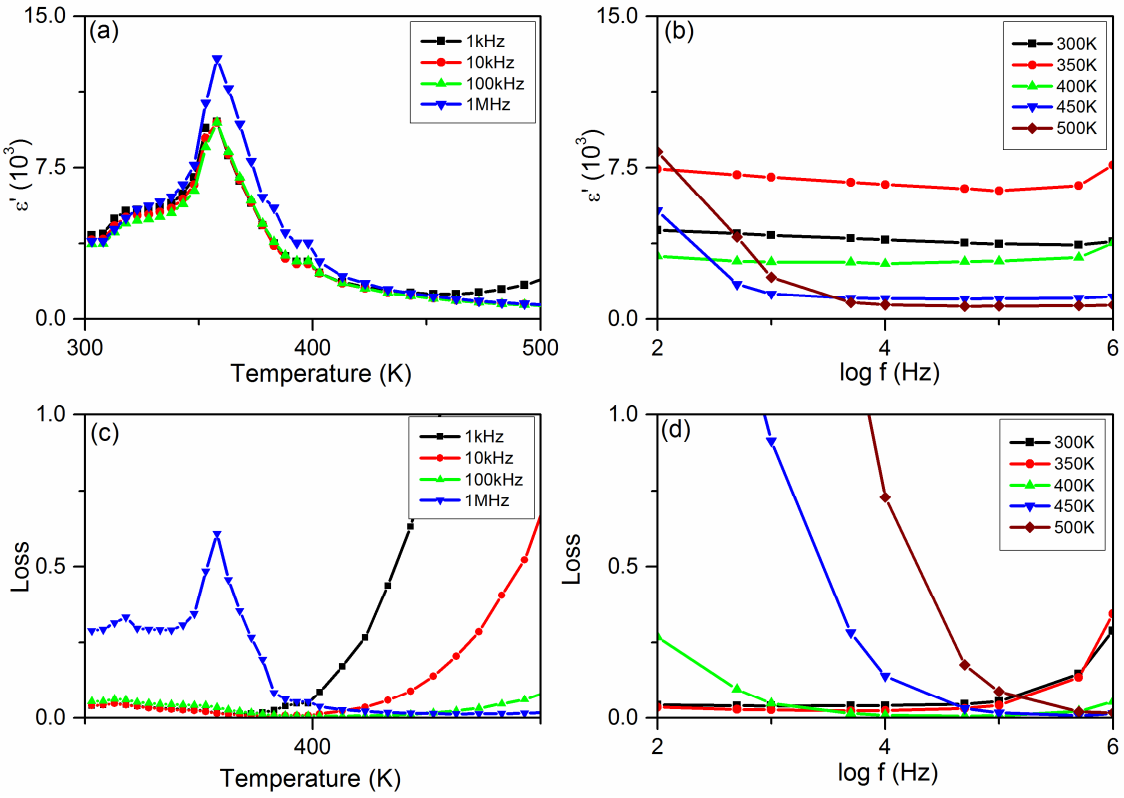

Figure 7.6: $BaTi_{1-x}Sn_xO_3$ (x = 0.05) plots of (a) Permittivity (ε′) vs. Temperature at various frequencies (b) Permittivity (ε′) vs. log f at various temperature (c) Dielectric loss vs. Temperature at various frequencies (d) Dielectric loss vs. log f at various temperatures.

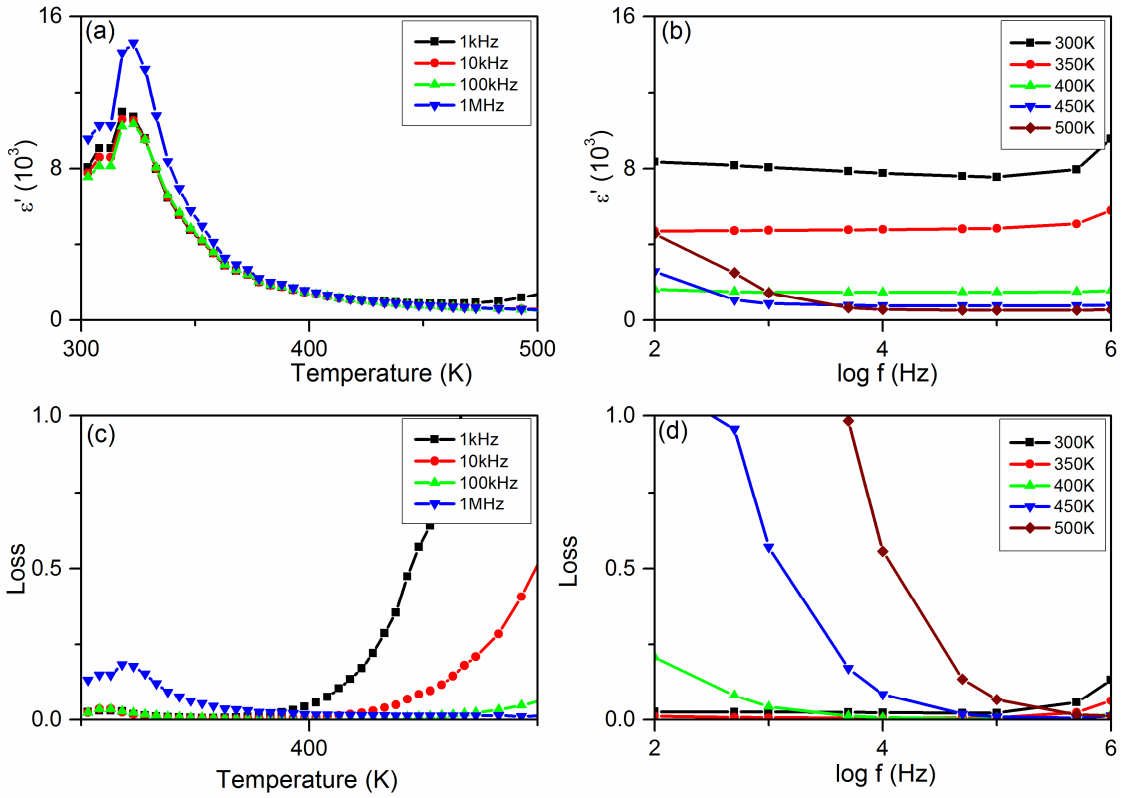

Figure 7.7: $BaTi_{1-x}Sn_xO_3$ (x = 0.10) plots of (a) Permittivity (ε′) vs. Temperature at various frequencies (b) Permittivity (ε′) vs. log f at various temperature (c) Dielectric loss vs. Temperature at various frequencies (d) Dielectric loss vs. log f at various temperatures.

Table 7.3: Dielectric Constant, Loss (at 1MHz, Room Temperature) and Temperature T_m corresponding to ε'_m

Composition(x)	**ε'_m**	**ε'_{RT}**	**loss**	**T_m(K)**
0.05	12912	3843	0.2	358
0.10	14614	9557	0.1	323
0.15	2254	2254	0.03	-

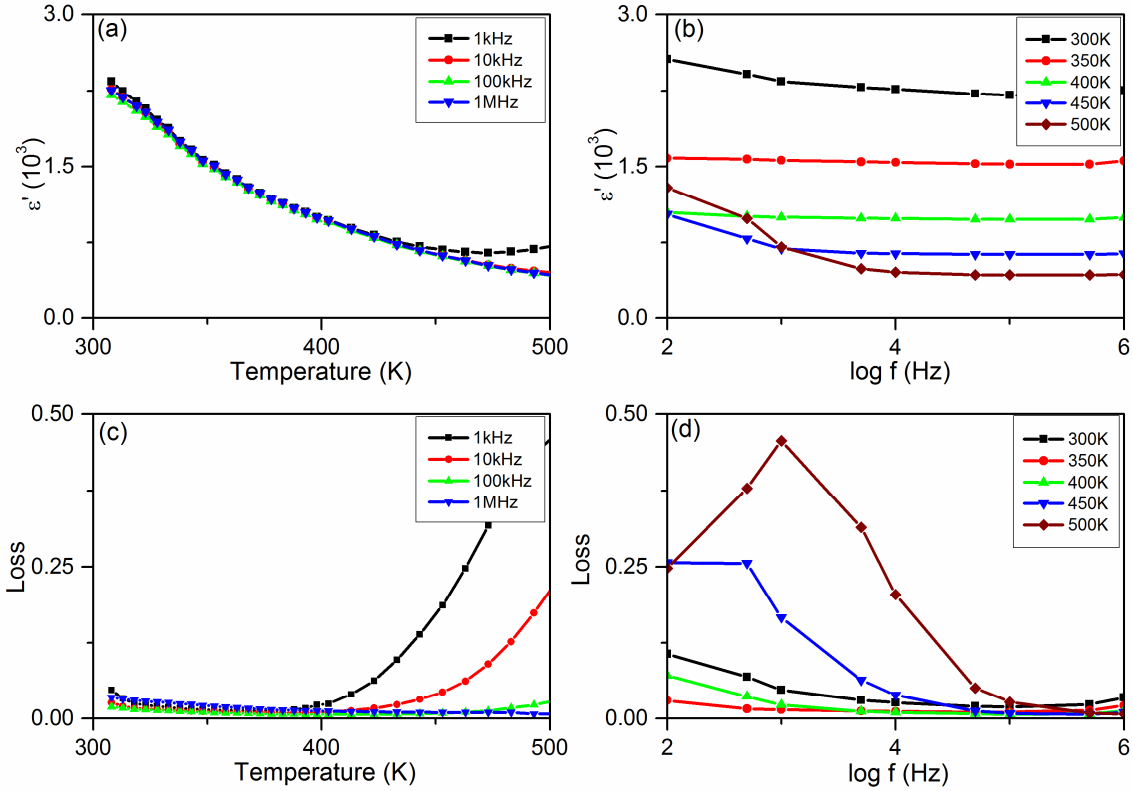

Figure 7.8 : $BaTi_{1-x}Sn_xO_3$ (x = 0.15) plots of (a) Permittivity (ε′) vs. Temperature at various frequencies (b) Permittivity (ε′) vs. log f at various temperature (c) Dielectric loss vs. Temperature at various frequencies (d) Dielectric loss vs. log f at various temperatures.

The permittivity peaks appear to be diffused. Coalescence of the low temperature phase transformations like rhombohedral to orthorhombic and orthorhombic to tetragonal leads to broadening of permittivity peak [yasuda et al. (1996)]. Also Sn doping tends to enhance diffuse phase transitions for x≤0.15 [Markovic et al. 2007]. In order to understand the nature of this broadening in our samples 1/ε′ vs. T was fitted in accordance with the Curie-Weiss law (Equation (7.1))

$$1/\varepsilon' = C/(T-T_C) \qquad \ldots(7.1)$$

where C is Curie constant(K^{-1}) and T_C is the Curie Temperature (K).

In BTS5 and BTS10, the data deviated from the Curie-Weiss law as shown in the Figures 7.6 (a,b). This is in agreement with the results reported by other researchers [Zhang et al. (2015); Markovic et al. (2007) and references therein] and indicates the

presence of diffuse phase transition (DPT). By using the high temperature linear portion of the graphs and a linear fit, the temperature at which the deviation starts (the so-called Burn's temperature, T_B) [Maso et al. (2006)] was obtained as indicated by dotted line in the aforementioned figures. The degree of diffuseness was estimated by fitting the experimental data to the modified Curie-Weiss law [Uchino et al. (1982)] (Equation (7.2))

$$1/\varepsilon' - 1/\varepsilon'_m = (T-T_m)^{\gamma} / C, \qquad (T > T_m) \qquad ...(7.2)$$

where ε'_m is the maximum permittivity , T_m is the corresponding temperature and γ is a measure of degree of diffusivity parameter. Here $\gamma = 1$ corresponds to normal ferroelectric phase transition, $\gamma = 2$ to the so called complete relaxor behaviour while $1 < \gamma < 2$ indicates Diffuse Phase Transition (DPT). The values of γ were obtained by fitting the experimental values of $\ln(1/\varepsilon' - 1/\varepsilon'_m)$ vs. $\ln(T-T_m)$ in accordance with Equation (7.2) in the temperature range T_m to T_B (Inset of Figures 7.9(a,b)).

The best fit values for ε'_m, T_m, γ and C were obtained at 100 kHz and are given in Table 7.3. The value of γ calculated above indicates that samples exhibit DPT behaviour which increases with Sn doping. It may be mentioned that displacive ferroelectrics such as barium titanate exhibit Curie constant of the order of 10^5 [Jaffe et al. (1971)]. Higher values of Curie constant are a signature of DPT [Uchino et al. (1982)]. BTS15 has a T_m below room temperature hence its analysis was not possible due to lack of sufficient experimental data.

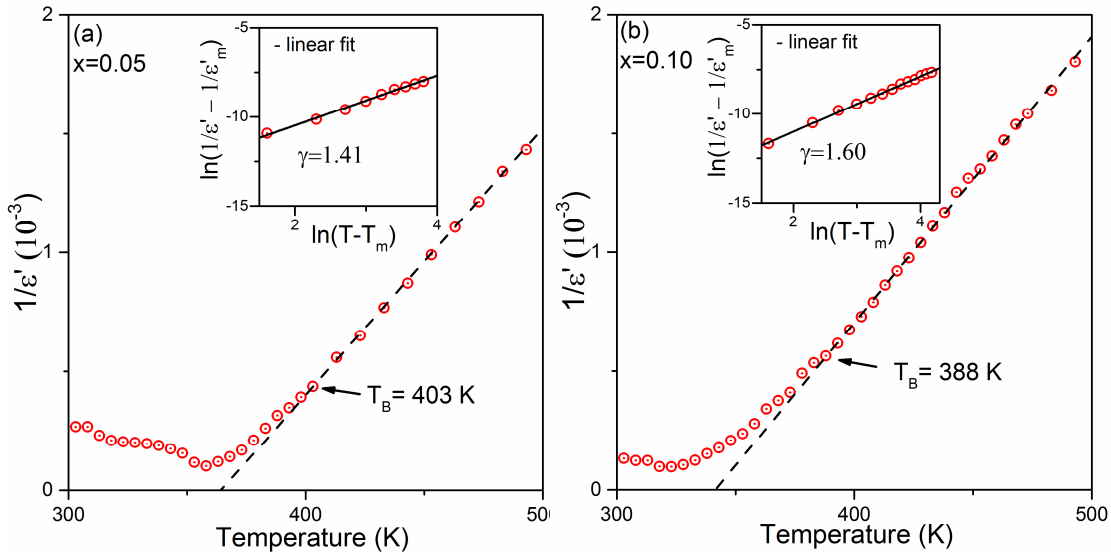

Figure 7.9: Inverse permittivity vs. temperature curve fitted according to Curie-Weiss law and $\ln(1/\varepsilon' - 1/\varepsilon'_m)$ vs. $\ln(T-T_m)$ curve fitted according to Modified Curie-Weiss law shown in inset for $BaTi_{1-x}Sn_xO_3$ (a) x = 0.05, (b) x=0.10.

Table 7.4: The best fit values for ε_m, T_m , γ and C at 100 kHz for $BaTi_{1-x}Sn_xO_3$ (x = 0.05 and 0.10) in accordance with modified Curie-Weiss Law (Equation (7.2))

Composition(x)	ε'_m	T_m (K)	T_B (K)	$\Delta T = T_B - T_m$	γ	C (10^6 K^{-1})
0.05	9710	358	403	45	1.41	0.59
0.10	10333	323	388	92	1.60	1.37

7.3.4 Impedance Spectroscopy

Complex impedance data were taken as a function of frequency and temperature for all the samples. They were analyzed and equivalent circuit models representing the behavior were obtained. As the paraelectric state of Sn doped barium titanate is more important application wise, attention was paid towards the high temperature data and equivalent circuit models were developed. Typical plots of Z'' vs. Z', Z' vs. log f and Z'' vs. log f for all the samples are shown in Figures 7.10(a,b) – 7.12(a,b). A grain – grain boundary – electrode system having three charge transfer processes with different

time constants can be the best visualization of an electrode ceramic sample [Moulson et al. (2003); Barsoukov et al. (2005)].

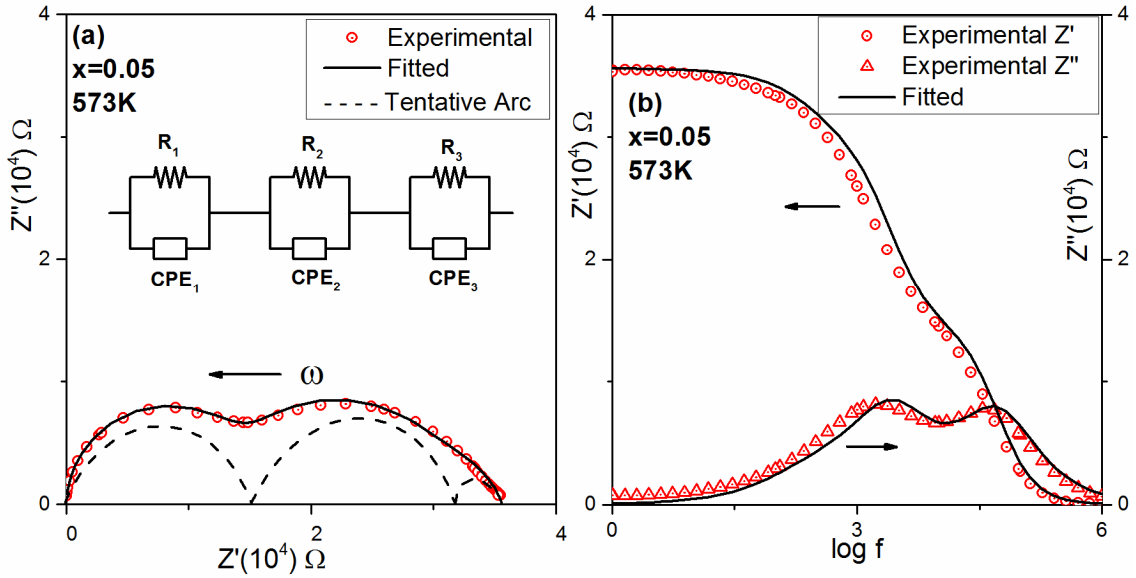

Figure 7.10: Experimental and fitted plots of (a) Z″ vs. Z′ and (b) Z′, Z″ vs. log f at 573 K for $BaTi_{1-x}Sn_xO_3$ (x = 0.05)

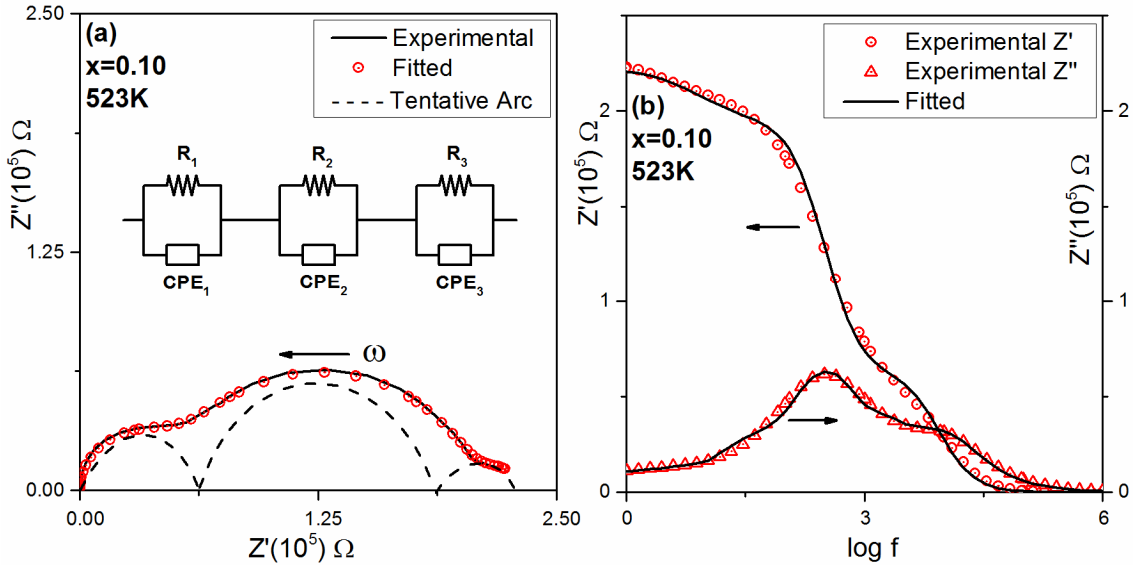

Figure 7.11: Experimental and fitted plots of (a) Z″ vs. Z′ and (b) Z′, Z″ vs. log f at 523 K for $BaTi_{1-x}Sn_xO_3$ (x = 0.10)

The impedance Z^* (= $Z' - j Z''$) of a series combination of parallel $R_1 – CPE_1$, parallel $R_2 – CPE_2$ and parallel $R_3 – CPE_3$ is given below [Pandey et al. (2017); Macdonald et al. (2005)]

$$Z^* = \frac{R_1}{1+ A_{01} R_1 (j\omega)^{\Psi_1}} + \frac{R_2}{1+ A_{02} R_2 (j\omega)^{\Psi_1}} + \frac{R_3}{1+ A_{03} R_3 (j\omega)^{\Psi_3}} \quad \ldots (7.3)$$

$$= \frac{R_1}{1+ (j\omega\tau_1)^{\Psi_1}} + \frac{R_2}{1+ (j\omega\tau_2)^{\Psi_1}} + \frac{R_3}{1+ (j\omega\tau_3)^{\Psi_3}} \quad \ldots (7.4)$$

where $\tau_1 = (A_{01} R_1)^{(1/\Psi 1)}$, $\Psi_1 = 1-\theta_1/(\pi/2)$ … (7.5)

. $\tau_2 = (A_{02} R_2)^{(1/\Psi 2)}$, $\Psi_2 = 1-\theta_2/(\pi/2)$ … (7.6)

. $\tau_3 = (A_{03} R_3)^{(1/\Psi 3)}$, $\Psi_3 = 1-\theta_3/(\pi/2)$ … (7.7)

A_{01},A_{02} and A_{03} are parameters which have dimension of capacitance when ψ's is equal to 1. θ_1, θ_2 and θ_3 are angles as described below. R_1, R_2 and R_3 are in ohms and τ_1, τ_2 and τ_3 are time constants in seconds.

Two distinct depressed semicircular arcs should appear in Z'' vs. Z' plot for an equivalent circuit model containing parallel R_1-CPE_1 and parallel R_2-CPE_2 circuits connected in series, when their response frequencies are widely separated. Assuming that response frequencies of R_1-CPE_1 are much higher than those of R_2-CPE_2, then θ_1 would be the angle between Z' axis and the line joining the centre, ($R_1/2$, $-(R_1/2)\tan\theta_1$), of the depressed circular arc corresponding to R_1-CPE_1, to the origin in the Z'' vs. Z' plot. This arc would pass through origin at the high frequency side and will intercept the Z' axis at the point (R_1,0) at the low frequency side. Then, θ_2 would be the angle between Z' axis and the line joining the centre ($R_2/2$, $-(R_2/2)\tan\theta_2$), of the depressed low frequency side circular arc corresponding to R_2-CPE_2, to the point (R_1,0). The overall low frequency intercept of this combination will be at the point ($R_1 + R_2$, 0). Similarly, if $R_3 – CPE_3$ having the largest time constant is also present in series in the

equivalent circuit, θ_3 would be the angle between Z' axis and the line joining the centre, ($R_3/2$,-($R_3/2$)tan θ_3), of the depressed lowest frequency side circular arc corresponding to R_3-CPE_3, to the point (R_1 + R_2, 0). The overall low frequency intercept of this combination will then be at the point (R_1 + R_2 +R_3, 0) and the Z″ vs. Z′ plot would contain three distinct clearly visible depressed arcs when the response times are widely separated [Pandey et al. (2017); Macdonald et al. (2005)].

Three joined tentative arcs (as shown in Figure 7.12(a)) were drawn to estimate the initial values of the parameters of Equation (7.3). By finding the intercepts on the Z′ axis, the coordinates of the centres of tentative depressed arcs and the frequencies where the Z″ peaks [Pandey et al. (2017)]. Using these as initial guesses, the values of the components were determined more accurately by using the EIS Spectrum Analyzer 1.0 software [Bondarenko et al. (2005)]. Data for all the samples were analyzed in this way and are given in Figures 7.10-7.12 along with their fitted values. Typical values of the components for all the samples are given in Tables 7.4 – 7.6. The values of χ^2 (indicating the goodness of fit) for all the samples are below 0.05.

Table 7.5: Values of the components of the model for BTS5

T (K)	**R_1 (kΩ)**	**ψ_1**	**A_{01} (10^{-10})**	**R_2 (kΩ)**	**Ψ_2**	**A_{02} (10^{-9})**	**R_3 (kΩ)**	**Ψ_3**	**A_{03} (10^{-6})**
523	36.4 ±0.84	0.99 ±0.05	2.7 ±0.18	107.41 ±1.17	0.83 ±0.03	21.99 ±0.68	95 ±8.04	0.67 ±0.02	2.14 ±0.13
573	14.32 ±0.22	0.98 ±0.03	2.5 ±0.10	14.84 ±0.42	0.94 ±0.01	6.97 ±0.58	6.46 ±0.88	0.79 ±0.03	0.38 ±0.10
623	2.11 ±0.02	0.99 ±0.01	2.34 ±0.53	2.91 ±0.02	0.90 ±0.02	8.65 ±0.56	0.6 ±0.08	0.59 ±0.09	28.89 ±1.85
673	0.8 ±0.01	0.91 ±0.01	6.97 ±0.21	0.66 ±0.01	0.89 ±0.03	11.37 ±0.61	0.21 ±0.02	0.64 ±0.04	46.2 ±1.43

Table 7.6: Values of the components of the model for BTS10

T (K)	R_1 (kΩ)	ψ_1	A_{01} (10^{-10})	R_2 (kΩ)	Ψ_2	A_{02} (10^{-9})	R_3 (kΩ)	Ψ_3	A_{03} (10^{-6})
523	61.8 ±2.94	0.99 ±0.01	3.01 ±0.17	132.20 ±3.84	0.99 ±0.01	4.02 ±0.46	29.00 ±1.60	0.8 ±0.11	1.49 ±0.11
573	15 ±1.17	0.88 ±0.05	3.95 ±0.14	16 ±2.17	0.95 ±0.02	1.04 ±0.09	2 ±0.07	0.95 ±0.01.	2.45 ±0.11
623	2.0 ±0.08	0.99 ±0.01	3.49 ±0.19	3.75 ±0.08	0.91 ±0.01	2.57 ±0.11	0.6 ±0.02	0.85 ±0.12	28.81 ±1.17
673	0.7 ±0.01	0.98 ±0.02	1.81 ±0.09	0.8 ±0.01	0.94 ±0.01	1.56 ±0.24	0.25 ±0.01	0.61 ±0.05	72.03 ±1.76

Table 7.7: Values of the components of the model for BTS15

T (K)	R_1 (kΩ)	ψ_1	A_{01} (10^{-10})	R_2 (kΩ)	Ψ_2	A_{02} (10^{-9})	R_3 (kΩ)	Ψ_3	A_{03} (10^{-9})
573	96.94 ±4.38	1.00 ±0.06	164.91 ±7.97	1500 ±14.91	0.95 ±0.01	2.89 ±0.08	1328.7 ±16.17	0.76 ±0.01	8.12 ±0.28
623	50 ±4.3	0.60 ±0.01	427.48 ±6.37	180 ±5.21	0.87 ±0.01	8.09 ±0.03	180 ±4.64	0.98 ±0.01	2.22 ±0.09
673	14.97 ±0.30	1 ±0.01	383.58 ±3.15	21.07 ±0.32	0.87 ±0.01	12.90 ±0.81	23.88 ±0.29	0.70 ±0.01	12.99 ±0.75
723	4.14 ±0.05	0.63 ±0.01	1000 ±70.33	4.47 ±0.06	0.81 ±0.01	20.14 ±1.25	3.20 ±0.05	0.87 ±0.01	2.88 ±0.25

7.3.5 P-E Hysteresis

The P-E hysteresis plots at an applied field up to 8 KV/cm are given in Figure 7.13 (a,b) for BTS5 and BTS10 respectively. Since the phase transition temperature for BTS15 is below room temperature [Markovic et al. (2007)], it does not exhibit a hysteresis at room temperature while the other samples show normal ferroelectric P vs E hysteresis behaviour. Increase in Sn content from 5% to 10% leads to slimming of the hysteresis loop, which is pretty evident from Figure 7.13 (a,b) [Upadhyay et al. (2014)]. The PE loops are not fully saturated probably due to leakage current but these are definitely tending towards saturation. The approximate saturation polarization (P_s),

retentivity (P_r) and coercivity (E_c) for all the samples are presented in Table 7.9. All the values decrease with increase in Sn content which can be due to the non-ferroelectric nature of the $BaSnO_3$. Addition of Sn into $BaTiO_3$ leads to reduction in the ferroelectricity or correlation between ferroelectric dipole, resulting in reduced polarization [Upadhyay et al. (2014)].

Table 7.8: Approximate Saturation Polarization (P_s), Retentivity (P_r) and Coercivity (E_c) for all the samples

x	Approximate Saturation Polarization (P_s) ($\mu C/cm^2$)	Retentivity (P_r) ($\mu C/cm^2$)	Coercivity (E_c) (KV/cm)
0.05	9.93	5.81	2.04
0.10	6.86	2.18	1.1

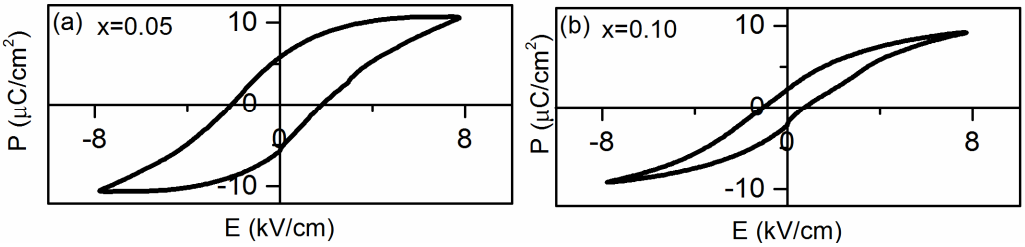

Figure 7.13: P-E Hysteresis loop for $BaTi_{1-x}Sn_xO_3$ (a) x = 0.05 and (b) x=0.10

7.3.6 Microwave range characterization

Figure 7.14 shows the variations of permittivity and dielectric loss in the frequency range 8 – 12 GHz measured at room temperature. Permittivity is almost independent of frequency and lies in the range 30-45 for all the samples in the frequency range 8-12 GHz. It is seen that addition of Sn leads to increase of permittivity in the above mentioned frequency range. Loss is also almost independent of frequency and lies between 0.10 – 0.30 for all the samples for this frequency range. The Dielectric measurements upto 67 GHz were reported for x= 0.02 thin film samples [Waldhoff

(2014)]. However, dielectric measurements in bulk systems in the microwave X –band are not available.

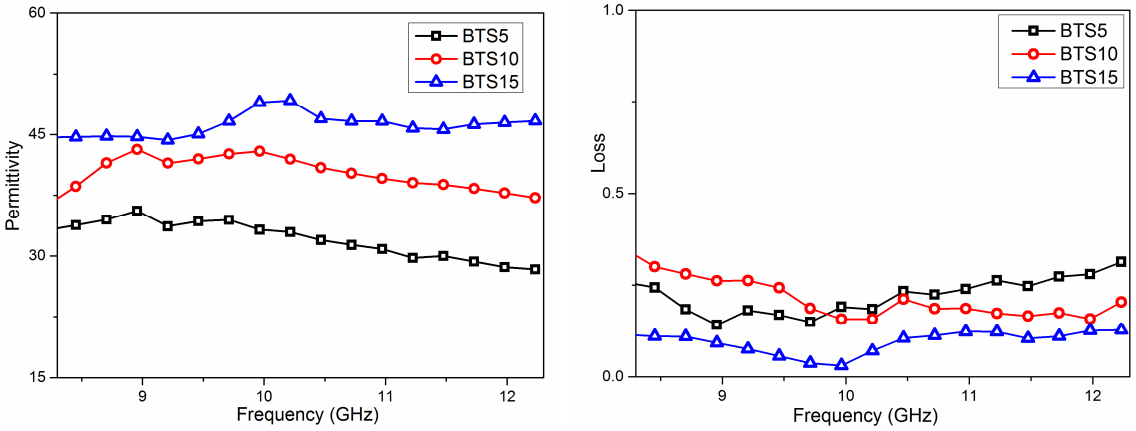

Figure 7.14 : Variation of (a) ε′ as function of frequency and (b) loss as function of frequency for $BaTi_{1-x}Sn_xO_3$ (x= 0.15) in X-Band(8 Ghz – 12 Ghz)

7.4 Conclusion

In conclusion compositions with x = 0.05, 0.10, and 0.15 in the system $Ba_{1-x}Sr_xTiO_3$ were synthesized using conventional solid state reaction method and characterized by XRD and SEM. Rietveld refinement of the XRD patterns confirmed the presence of single tetragonal phase for all BTS5 and BTS10 while BTS15 exists in cubic phase. Dielectric and impedance measurements were carried out in the temperature range 300K – 723 K. As x increases the temperature of permittivity maxima decreases almost linearly. The samples exhibit diffuse phase transition. An equivalent circuit model comprising three parallel combinations of resistance and constant phase angle element viz. $(R_1 – CPE_1) – (R_2\text{-}CPE_2) – (R_3\text{-}CPE_3)$, corresponding to grain, grain boundary and electrodes, was developed that represented the data well. This may be useful in design and simulation studies. P vs. E loops for the samples indicate a normal ferroelectric behaviour for BTS5 and BTS10. The values of dielectric permittivity measured in the frequency range 8-12 GHz in the X band of microwaves are around 30-45 for the samples and are almost independent of frequency with the loss being in the range 0.10 – 0.30